Frontiers of Information Technology & Electronic Engineering
www.jzus.zju.edu.cn; engineering.cae.cn; www.springerlink.com
ISSN 2095-9184 (print); ISSN 2095-9230 (online)
E-mail: jzus@zju.edu.cn

A parasitic coupling network concept for mutual coupling utilization in wideband multielement antenna arrays*#

Xiaojun ZOU†1, Guangming WANG2, Yawei WANG2, Wei SONG1, Hang ZHU1, Ming TAN1, Xuguang XU1, Guoqin KANG1, Binfeng ZONG†‡2

[1]College of Information and Communication, National University of Defense Technology, Wuhan 430035, China
[2]Air and Missile Defense College, Air Force Engineering University, Xi'an 710051, China
†E-mail: zouxj0606@163.com; zongbinfeng@163.com

Received Oct. 31, 2023; Revision accepted Mar. 20, 2024; Crosschecked Apr. 10, 2025

Abstract: A novel approach to widening the active reflection coefficient (ARC) bandwidth of an antenna array, employing a parasitic coupling network (PCN), is investigated in this article. Different from traditional tightly coupled arrays adopting space structures for enhancing the coupling in balanced-excitation antennas, a PCN derived from rigorous formulas is employed in the feeding lines of unbalanced-excitation ones. Based on network analysis, the mutual coupling utilization condition for an (M×N)-element antenna array is initially deduced, and the PCN is implemented. Then, the PCNs are realized by introducing a parasitic element and a coupling network between the two-element H-plane and E-plane dual-layer coupled microstrip antenna arrays, resulting in 10.9% and 30.8% bandwidth enhancements compared with the original arrays, respectively. Moreover, the PCNs are further expanded to multielement antenna arrays, including three- and five-element one-dimensional and 8×2 two-dimensional arrays, exhibiting approximately 40% overlapped ARC bandwidths with normal radiation patterns, steady gains, and applicable scanning characteristics. The results indicate its potential application in large-scale wideband arrays.

Key words: Active reflection coefficient (ARC); Antenna array; Parasitic coupling network (PCN); Scanning array; Wideband
https://doi.org/10.1631/FITEE.2300742 **CLC number:** TN823

1 Introduction

Mutual coupling manipulation is always an awkward issue for antenna array design, as coupling between array elements can trigger the deterioration of antenna performance, including impedance matching, radiation pattern, gain, sidelobe level, and scanning characteristics (Allen and Diamond, 1966; Guo et al., 2020). Therefore, many studies have been carried out on suppressing mutual coupling, and plentiful techniques have been proposed to achieve high isolation between elements, which can be divided mainly into two categories. One category is field methods, such as defected ground structure (DGS) (Kumar C et al., 2017), frequency selective surface (FSS) (Zhu et al., 2021), electromagnetic bandgap (EBG) (Zhai et al., 2016), single negative (SNG) metamaterial (Bait-Suwailam et al., 2010) and metasurface (Liu et al., 2020), array-antenna decoupling surface (ADS) (Wu et al., 2017), and parasitic decoupling (Lau and Andersen, 2012; Ghadimi et al., 2020; Kumar P et al., 2023). Here, parasitic decoupling mainly reduces mutual coupling by introducing parasitic structures between array elements to counteract the coupling field or current; thus,

‡ Corresponding author
* Project supported by the National Natural Science Foundation of China (Nos. 62201579 and 62201580) and the Youth Independent Innovation Science Foundation of National University of Defense Technology (No. ZK24-39)
# Electronic supplementary materials: The online version of this article (https://doi.org/10.1631/FITEE.2300742) contains supplementary materials, which are available to authorized users
ORCID: Xiaojun ZOU, https://orcid.org/0000-0003-3883-7255; Binfeng ZONG, https://orcid.org/0000-0003-3399-5756

the radiation performance can be greatly improved. The other category is circuit methods, covering decoupling networks (Zou et al., 2019, 2023; Wang ZT and Wu, 2023) and neutralization lines (Li M et al., 2020). However, mutual coupling can also be used to improve the antenna performance. According to the operating mechanism of the loaded structure, mutual coupling utilization methods can be divided into space and network ones.

The most typical example of space mutual coupling utilization is a tightly coupled array (TCA), the concept of which is derived from the infinite current sheet array (CSA) proposed by Wheeler (1965) and developed by Munk et al. (2003), who discovered that, through introducing coupling components to the end of the closely arranged dipoles, the antenna array could exhibit wideband characteristic. Since then, copious works concerning TCA have been carried out to expand the bandwidth of the antenna array and wide-angle scanning range (Holland and Vouvakis, 2012; Chen et al., 2021; Li WT et al., 2023; Zhang et al., 2023). After initially being employed in dipole arrays, TCA has been further expanded to other balanced-excitation antenna arrays, the elements of which are usually symmetric with two arms and are fed by the same amplitude and a 180° phase difference (Holland and Vouvakis, 2012), including Vivaldi array (Reid et al., 2012) and spiral antenna array (Alwan et al., 2012). However, for unbalanced-excitation antennas, the concept of mutual coupling utilization is scarcely introduced.

Network coupling utilization mainly involves a strong coupling structure (Qu et al., 2013) and an overlapped feeding network (Xia et al., 2014). The former mainly exists in sparse arrays, which can retain a similar aperture efficiency, simplify the feeding network, and reduce the total cost by intentionally connecting adjacent array elements to strengthen the mutual coupling. These arrays can be equivalent to circuit models and be analyzed according to the network theory, but the scanning characteristics still require exploration. However, the latter is scarcely reported, and the overlapped feeding network was introduced to enhance the coupling between array elements, improve the active reflection coefficient (ARC), and widen the scan angles to ±60° (Xia et al., 2014). However, the decoupling network, which is frequently introduced to eliminate mutual coupling between elements, is also a vital approach from the perspective of network analysis. The coupling matrix was extracted from the two-port network to deduce the decoupling and matching conditions (Zhao et al., 2014). By adding a parasitic port, novel and efficient parasitic decoupling networks were presented to achieve high isolation (Li M et al., 2019). Also, the decoupling and matching network was designed by rigorous formulas upon the scattering matrix and was optimized using the binary optimization algorithm (Li M et al., 2022a). Additionally, based on *S*-parameters and radiation patterns, a hybrid network was conducted for multiple-input multiple-output systems using the *N*-ary optimization algorithm (Li M et al., 2022b). Since the network analysis is precise and general and has potential, the design of the decoupling network can be stretched to that of a coupling network for mutual coupling utilization, which has rarely been reported.

In this article, targeting the network structure design and unbalanced-excitation antenna, an efficient parasitic coupling network (PCN) is proposed to improve the performance of a dual-layer coupled microstrip antenna array. First, on the basis of the network model, the mutual coupling utilization condition for an (M×N)-element antenna array is built in Section 2. The PCN implementation is also derived from an (M×N)-port network and its scattering parameters. Then, in Section 3, a parasitic element and a coupling network, comprising the proposed PCN, are respectively inserted between elements and the feeding lines of the H-plane coupled antenna array. In addition, the PCN is employed in an E-plane coupled array and is further extended to multielement arrays, including three- and five-element one-dimensional and 8×2 two-dimensional arrays. The results demonstrate that all arrays have approximately 40% overlapped ARC bandwidths, normal radiation patterns, steady gains, and applicable scanning characteristics. Finally, conclusions are drawn in Section 4. The novelty and contributions of the proposed PCN are described as follows:

1. The parasitic network is traditionally employed in antenna decoupling, but the PCN breaks the limitation and is expanded to the mutual coupling utilization.

2. An unbalanced-excitation antenna, i.e., a dual-layer coupled microstrip antenna, is selected as the basic element for the coupling utilization; previously,

balanced-excitation antennas have been the most common.

3. The PCN design is simple to follow, and it is easy to judge whether the mutual coupling can be used or not according to the derived mutual coupling utilization condition for the planar large-scale multielement antenna array.

4. The PCN is practical for both one- and two-dimensional wideband antenna arrays, and has potential for use with large-scale arrays.

2 Operating principle of PCN

2.1 Mutual coupling utilization condition

To deduce the mutual coupling utilization condition, an (M×N)-port network is constructed to represent an antenna array with M×N elements, as depicted in Fig. 1a. Assume that the radiation, heat loss, and resonant storage are deemed the energy dissipated in the network, and the mutual coupling between elements mostly reflects the variation of scattering coefficients. According to the scattering matrix of the multi-port network, the normalized reflected wave of element (m, n) (m=1, 2, ⋯, M; n=1, 2, ⋯, N) at port (m, n) is

$$b_{(m,n)} = S_{(m,n),(1,1)}a_{(1,1)} + S_{(m,n),(1,2)}a_{(1,2)} + \cdots + S_{(m,n),(m,n)}a_{(m,n)} + \cdots + S_{(m,n),(M,N)}a_{(M,N)}, \quad (1)$$

where $a_{(p,q)}$ ($p\in\{1, 2, \cdots, M\}$, $q\in\{1, 2, \cdots, N\}$) is the normalized incident wave at port (p, q) and $S_{(m,n),(p,q)}$ is the scattering coefficient related to element (m, n), both of which contain the corresponding magnitude and phase. Thus, when all the array elements work, the ARC of element (m, n) can be expressed as (Kahn, 1969)

$$S_{(m,n),(m,n)\text{active}}=\sum_{p=1}^{M}\sum_{q=1}^{N}\frac{a_{(p,q)}}{a_{(m,n)}}S_{(m,n),(p,q)}. \quad (2)$$

It can be inferred from Eq. (2) that, when all the elements are excited with the same magnitude and phase (i.e., $a_{(1,1)}=a_{(1,2)}=\cdots=a_{(m,n)}=\cdots=a_{(M,N)}$), the ARC of element ($m$, n) becomes the sum of the reflection coefficient $S_{(m,n),(m,n)}$ and coupling coefficients $S_{(m,n),(p,q)}$ between port (m, n) and other ports, that is,

$$S_{(m,n),(m,n)\text{active}} = S_{(m,n),(1,1)} + S_{(m,n),(1,2)} + \cdots + S_{(m,n),(m,n)} + \cdots + S_{(m,n),(M,N)}. \quad (3)$$

For a scanning array with scan angle (θ, φ), the feeding phase differences between adjacent elements with the distances of d_x and d_y in the two dimensions are $\psi_x=kd_x\sin\theta\cos\varphi$ and $\psi_y=kd_y\sin\theta\sin\varphi$. Then $a_{(p,q)}=a_{(m,n)}e^{-j[(p-m)\psi_x+(q-n)\psi_y]}$, that is,

$$S_{(m,n),(m,n)\text{active}}=\sum_{p=1}^{M}\sum_{q=1}^{N}S_{(m,n),(p,q)}e^{-j[(p-m)\psi_x+(q-n)\psi_y]}. \quad (4)$$

Fig. 1b presents the calculation of the ARC. According to the relationship between the reflection coefficient and the coupling coefficient circles, it is evident that, when the phase difference $\Delta\varphi$ between the reflection coefficient and the sum of coupling coefficients varies in the angle range marked in yellow, the magnitude of the ARC will be no greater than that of the reflection coefficient, that is, $|S_{(m,n),(m,n)\text{active}}|\leqslant|S_{(m,n),(m,n)}|$; then, the mutual coupling can contribute to the improvement of the array performance. Conversely, the coupling will deteriorate the performance. Thus, the mutual coupling utilization condition can be developed from a two-port network (Wang YW and Yu, 2017) and can be determined as

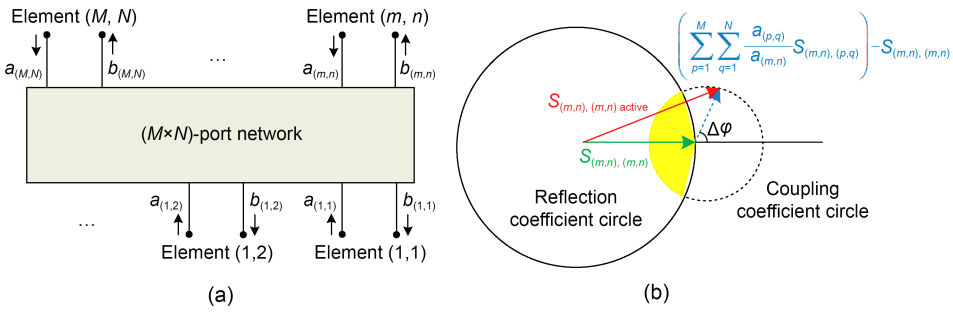

Fig. 1 Analysis of the mutual coupling utilization condition: (a) network model; (b) calculation of the active reflection coefficient (ARC). References to color refer to the online version of this figure

$$\pi-\arccos\left(\frac{\left|\left(\sum_{p=1}^{M}\sum_{q=1}^{N}\frac{a_{(p,q)}}{a_{(m,n)}}S_{(m,n),(p,q)}\right)-S_{(m,n),(m,n)}\right|}{2\left|S_{(m,n),(m,n)}\right|}\right)\le\Delta\varphi$$
$$\le\pi+\arccos\left(\frac{\left|\left(\sum_{p=1}^{M}\sum_{q=1}^{N}\frac{a_{(p,q)}}{a_{(m,n)}}S_{(m,n),(p,q)}\right)-S_{(m,n),(m,n)}\right|}{2\left|S_{(m,n),(m,n)}\right|}\right), \tag{5}$$

where the constitutive condition is

$$\left|\left(\sum_{p=1}^{M}\sum_{q=1}^{N}\frac{a_{(p,q)}}{a_{(m,n)}}S_{(m,n),(p,q)}\right)-S_{(m,n),(m,n)}\right|\le 2\left|S_{(m,n),(m,n)}\right|. \tag{6}$$

If the constitutive condition is not satisfied, data will be missing in the upper and lower boundaries, and the coupling utilization should be evaluated according to the specific circumstance. Inequality (5) accounts for why the balanced-excitation antenna array can better use mutual coupling between its elements, as when the elements are excited with the same magnitude and phase, the phase difference $\Delta\varphi$ approaches 180°, and the superposition of the reflection coefficient and coupling coefficients can always fall in the yellow range; thus, it will gain a smaller magnitude. However, for the unbalanced-excitation antenna array, the situation becomes complex, considering that the phase difference is out of control. Thus, one specific geometry can be inserted to manipulate the mutual coupling for the purpose of performance enhancement.

2.2 PCN implementation

The proposed PCN is conducted by introducing parasitic elements between array elements to couple energy from antennas, and then the parasitic elements are connected to coupling networks between feeding lines to guide the coupled energy, enhancing the coupling between array elements; thus, mutual coupling can be used. For an ($M\times N$)-element antenna array loaded with PCN, its overall equivalent network model can be represented in Fig. 2a, which can be analyzed from two split parts, as demonstrated in Fig. 2b. For simplicity, only the front two antennas are displayed to concretely denote the port definitions. The upper part is an ($M\times N$)-port network, indicating the original coupled antenna array, whose scattering matrix $\boldsymbol{S}^{\mathrm{A}}$ is as Eq. (7) (on the next page); the lower part is a ($4M\times N-M-N$)-port network via introducing $T=M\times(N-1)+(M-1)\times N$ PCNs connected with parasitic elements and its scattering matrix $\boldsymbol{S}^{\mathrm{P}}$ is represented by Eq. (8) (on the next page). Here, $a^{\mathrm{A}}_{(m,n)\mathrm{a}}$ and $b^{\mathrm{A}}_{(m,n)\mathrm{a}}$ are the incident and reflected waves of the original array; ($a^{\mathrm{P}}_{(m,n)}$, $a^{\mathrm{P}}_{(m,n)\mathrm{a}}$, a^{P}_{ie}) and ($b^{\mathrm{P}}_{(m,n)}$, $b^{\mathrm{P}}_{(m,n)\mathrm{a}}$, b^{P}_{ie}) are those of the lower network, connected with the feeding port, the antenna element, and the parasitic element, respectively. ($S^{\mathrm{A}}_{(m,n)\mathrm{a},(m,n)\mathrm{a}}$, $S^{\mathrm{P}}_{(m,n),(m,n)}$, $S^{\mathrm{P}}_{(m,n)\mathrm{a},(m,n)\mathrm{a}}$, $S^{\mathrm{P}}_{ie,ie}$) and ($S^{\mathrm{A}}_{(m,n)\mathrm{a},(p,q)\mathrm{a}}$, $S^{\mathrm{P}}_{(m,n),(p,q)}$, $S^{\mathrm{P}}_{(m,n)\mathrm{a},(p,q)\mathrm{a}}$, $S^{\mathrm{P}}_{ie,je}$) are the reflection and coupling coefficients of the coupled array and the PCN respectively, and $S^{\mathrm{P}}_{(m,n),(p,q)\mathrm{a}}$, $S^{\mathrm{P}}_{(m,n),je}$, $S^{\mathrm{P}}_{(m,n)\mathrm{a},(p,q)}$, $S^{\mathrm{P}}_{(m,n)\mathrm{a},je}$, $S^{\mathrm{P}}_{ie,(p,q)}$, and $S^{\mathrm{P}}_{ie,(p,q)\mathrm{a}}$ are the internal transmission coefficients of the PCN, which all contain magnitudes and phases. When the upper network is cascaded with the lower one, according to the incident and reflected relations in Fig. 2b, Eq. (7) can be transformed into Eq. (9) (on the next page).

By substituting Eq. (9) into Eq. (8), the PCN can be reduced to a ($3M\times N-M-N$)-port network, including $M\times N$ feeding ports and T parasitic ports. Then, the scattering matrix $\boldsymbol{S}^{\mathrm{R}}$ is simplified as Eq. (10) (on the next page).

Considering that each parasitic port is connected with a parasitic element whose scattering coefficient satisfies $b^{\mathrm{E}}_{ie}=S^{\mathrm{E}}_{i}a^{\mathrm{E}}_{ie}$ (a and b are the incident and reflected waves of the parasitic element), there is $b^{\mathrm{P}}_{ie}=a^{\mathrm{P}}_{ie}/S^{\mathrm{E}}_{i}$. The eventual ($M\times N$)-port scattering matrix $\boldsymbol{S}^{\mathrm{C}}$, representing the whole network, can be obtained as Eq. (11) (on the next page).

From Eqs. (10) and (11), the ultimate matrix of the antenna array with the PCN $\boldsymbol{S}^{\mathrm{C}}$ can be achieved, as the scattering matrix of the original coupled antenna array $\boldsymbol{S}^{\mathrm{A}}$ is known, and that of the lower network $\boldsymbol{S}^{\mathrm{P}}$ can be conveniently tuned via changing the dimensions of the coupling network and acquired through simulation or measurement, as well as by adjusting the dimensions of parasitic element S^{E}_{i}. It is noted that all the scattering parameters contain magnitude and phase; then, according to inequality (5), the mutual coupling utilization condition of the antenna array with the PCN can be further achieved.

$$\begin{bmatrix} b^{\mathrm{A}}_{(1,1)\mathrm{a}} \\ b^{\mathrm{A}}_{(1,2)\mathrm{a}} \\ \vdots \\ b^{\mathrm{A}}_{(M,N)\mathrm{a}} \end{bmatrix} = \boldsymbol{S}^{\mathrm{A}} \begin{bmatrix} a^{\mathrm{A}}_{(1,1)\mathrm{a}} \\ a^{\mathrm{A}}_{(1,2)\mathrm{a}} \\ \vdots \\ a^{\mathrm{A}}_{(M,N)\mathrm{a}} \end{bmatrix} = \begin{bmatrix} S^{\mathrm{A}}_{(1,1)\mathrm{a},(1,1)\mathrm{a}} & S^{\mathrm{A}}_{(1,1)\mathrm{a},(1,2)\mathrm{a}} & \cdots & S^{\mathrm{A}}_{(1,1)\mathrm{a},(M,N)\mathrm{a}} \\ S^{\mathrm{A}}_{(1,2)\mathrm{a},(1,1)\mathrm{a}} & S^{\mathrm{A}}_{(1,2)\mathrm{a},(1,2)\mathrm{a}} & \cdots & S^{\mathrm{A}}_{(1,2)\mathrm{a},(M,N)\mathrm{a}} \\ \vdots & \vdots & & \vdots \\ S^{\mathrm{A}}_{(M,N)\mathrm{a},(1,1)\mathrm{a}} & S^{\mathrm{A}}_{(M,N)\mathrm{a},(1,2)\mathrm{a}} & \cdots & S^{\mathrm{A}}_{(M,N)\mathrm{a},(M,N)\mathrm{a}} \end{bmatrix} \begin{bmatrix} a^{\mathrm{A}}_{(1,1)\mathrm{a}} \\ a^{\mathrm{A}}_{(1,2)\mathrm{a}} \\ \vdots \\ a^{\mathrm{A}}_{(M,N)\mathrm{a}} \end{bmatrix}. \tag{7}$$

$$\begin{aligned} &\left[b^{\mathrm{P}}_{(1,1)}, \cdots, b^{\mathrm{P}}_{(M,N)}, b^{\mathrm{P}}_{(1,1)\mathrm{a}}, \cdots, b^{\mathrm{P}}_{(M,N)\mathrm{a}}, b^{\mathrm{P}}_{1\mathrm{e}}, \cdots, b^{\mathrm{P}}_{T\mathrm{e}} \right]^{\mathrm{T}} = \boldsymbol{S}^{\mathrm{P}} \left[a^{\mathrm{P}}_{(1,1)}, \cdots, a^{\mathrm{P}}_{(M,N)}, a^{\mathrm{P}}_{(1,1)\mathrm{a}}, \cdots, a^{\mathrm{P}}_{(M,N)\mathrm{a}}, a^{\mathrm{P}}_{1\mathrm{e}}, \cdots, a^{\mathrm{P}}_{T\mathrm{e}} \right]^{\mathrm{T}} \\ &= \begin{bmatrix} S^{\mathrm{P}}_{(1,1),(1,1)} & \cdots & S^{\mathrm{P}}_{(1,1),(M,N)} & S^{\mathrm{P}}_{(1,1),(1,1)\mathrm{a}} & \cdots & S^{\mathrm{P}}_{(1,1),(M,N)\mathrm{a}} & S^{\mathrm{P}}_{(1,1),1\mathrm{e}} & \cdots & S^{\mathrm{P}}_{(1,1),T\mathrm{e}} \\ \vdots & & \vdots & \vdots & & \vdots & \vdots & & \vdots \\ S^{\mathrm{P}}_{(M,N),(1,1)} & \cdots & S^{\mathrm{P}}_{(M,N),(M,N)} & S^{\mathrm{P}}_{(M,N),(1,1)\mathrm{a}} & \cdots & S^{\mathrm{P}}_{(M,N),(M,N)\mathrm{a}} & S^{\mathrm{P}}_{(M,N),1\mathrm{e}} & \cdots & S^{\mathrm{P}}_{(M,N),T\mathrm{e}} \\ S^{\mathrm{P}}_{(1,1)\mathrm{a},(1,1)} & \cdots & S^{\mathrm{P}}_{(1,1)\mathrm{a},(M,N)} & S^{\mathrm{P}}_{(1,1)\mathrm{a},(1,1)\mathrm{a}} & \cdots & S^{\mathrm{P}}_{(1,1)\mathrm{a},(M,N)\mathrm{a}} & S^{\mathrm{P}}_{(1,1)\mathrm{a},1\mathrm{e}} & \cdots & S^{\mathrm{P}}_{(1,1)\mathrm{a},T\mathrm{e}} \\ \vdots & & \vdots & \vdots & & \vdots & \vdots & & \vdots \\ S^{\mathrm{P}}_{(M,N)\mathrm{a},(1,1)} & \cdots & S^{\mathrm{P}}_{(M,N)\mathrm{a},(M,N)} & S^{\mathrm{P}}_{(M,N)\mathrm{a},(1,1)\mathrm{a}} & \cdots & S^{\mathrm{P}}_{(M,N)\mathrm{a},(M,N)\mathrm{a}} & S^{\mathrm{P}}_{(M,N)\mathrm{a},1\mathrm{e}} & \cdots & S^{\mathrm{P}}_{(M,N)\mathrm{a},T\mathrm{e}} \\ S^{\mathrm{P}}_{1\mathrm{e},(1,1)} & \cdots & S^{\mathrm{P}}_{1\mathrm{e},(M,N)} & S^{\mathrm{P}}_{1\mathrm{e},(1,1)\mathrm{a}} & \cdots & S^{\mathrm{P}}_{1\mathrm{e},(M,N)\mathrm{a}} & S^{\mathrm{P}}_{1\mathrm{e},1\mathrm{e}} & \cdots & S^{\mathrm{P}}_{1\mathrm{e},T\mathrm{e}} \\ \vdots & & \vdots & \vdots & & \vdots & \vdots & & \vdots \\ S^{\mathrm{P}}_{T\mathrm{e},(1,1)} & \cdots & S^{\mathrm{P}}_{T\mathrm{e},(M,N)} & S^{\mathrm{P}}_{T\mathrm{e},(1,1)\mathrm{a}} & \cdots & S^{\mathrm{P}}_{T\mathrm{e},(M,N)\mathrm{a}} & S^{\mathrm{P}}_{T\mathrm{e},1\mathrm{e}} & \cdots & S^{\mathrm{P}}_{T\mathrm{e},T\mathrm{e}} \end{bmatrix} \begin{bmatrix} a^{\mathrm{P}}_{(1,1)} \\ \vdots \\ a^{\mathrm{P}}_{(M,N)} \\ a^{\mathrm{P}}_{(1,1)\mathrm{a}} \\ \vdots \\ a^{\mathrm{P}}_{(M,N)\mathrm{a}} \\ a^{\mathrm{P}}_{1\mathrm{e}} \\ \vdots \\ a^{\mathrm{P}}_{T\mathrm{e}} \end{bmatrix}. \end{aligned} \tag{8}$$

$$\left[b^{\mathrm{P}}_{(1,1)\mathrm{a}}, b^{\mathrm{P}}_{(1,2)\mathrm{a}}, \cdots, b^{\mathrm{P}}_{(M,N)\mathrm{a}} \right]^{\mathrm{T}} = \left(\boldsymbol{S}^{\mathrm{A}} \right)^{-1} \left[a^{\mathrm{P}}_{(1,1)\mathrm{a}}, a^{\mathrm{P}}_{(1,2)\mathrm{a}}, \cdots, a^{\mathrm{P}}_{(M,N)\mathrm{a}} \right]^{\mathrm{T}}. \tag{9}$$

$$\begin{aligned} \begin{bmatrix} b^{\mathrm{R}}_{(1,1)} \\ \vdots \\ b^{\mathrm{R}}_{(M,N)} \\ b^{\mathrm{R}}_{1\mathrm{e}} \\ \vdots \\ b^{\mathrm{R}}_{T\mathrm{e}} \end{bmatrix} = \boldsymbol{S}^{\mathrm{R}} \begin{bmatrix} a^{\mathrm{R}}_{(1,1)} \\ \vdots \\ a^{\mathrm{R}}_{(M,N)} \\ a^{\mathrm{R}}_{1\mathrm{e}} \\ \vdots \\ a^{\mathrm{R}}_{T\mathrm{e}} \end{bmatrix} = &\left\{ \begin{bmatrix} S^{\mathrm{P}}_{(1,1),(1,1)\mathrm{a}} & \cdots & S^{\mathrm{P}}_{(1,1),(M,N)\mathrm{a}} \\ \vdots & & \vdots \\ S^{\mathrm{P}}_{(M,N),(1,1)\mathrm{a}} & \cdots & S^{\mathrm{P}}_{(M,N),(M,N)\mathrm{a}} \\ S^{\mathrm{P}}_{1\mathrm{e},(1,1)\mathrm{a}} & \cdots & S^{\mathrm{P}}_{1\mathrm{e},(M,N)\mathrm{a}} \\ \vdots & & \vdots \\ S^{\mathrm{P}}_{T\mathrm{e},(1,1)\mathrm{a}} & \cdots & S^{\mathrm{P}}_{T\mathrm{e},(M,N)\mathrm{a}} \end{bmatrix} \left(\left(\boldsymbol{S}^{\mathrm{A}} \right)^{-1} - \begin{bmatrix} S^{\mathrm{P}}_{(1,1)\mathrm{a},(1,1)\mathrm{a}} & \cdots & S^{\mathrm{P}}_{(1,1)\mathrm{a},(M,N)\mathrm{a}} \\ \vdots & & \vdots \\ S^{\mathrm{P}}_{(M,N)\mathrm{a},(1,1)\mathrm{a}} & \cdots & S^{\mathrm{P}}_{(M,N)\mathrm{a},(M,N)\mathrm{a}} \end{bmatrix} \right)^{-1} \\ &\cdot \begin{bmatrix} S^{\mathrm{P}}_{(1,1)\mathrm{a},(1,1)} & \cdots & S^{\mathrm{P}}_{(1,1)\mathrm{a},(M,N)} & S^{\mathrm{P}}_{(1,1)\mathrm{a},1\mathrm{e}} & \cdots & S^{\mathrm{P}}_{(1,1)\mathrm{a},T\mathrm{e}} \\ \vdots & & \vdots & \vdots & & \vdots \\ S^{\mathrm{P}}_{(M,N)\mathrm{a},(1,1)} & \cdots & S^{\mathrm{P}}_{(M,N)\mathrm{a},(M,N)} & S^{\mathrm{P}}_{(M,N)\mathrm{a},1\mathrm{e}} & \cdots & S^{\mathrm{P}}_{(M,N)\mathrm{a},T\mathrm{e}} \end{bmatrix} \\ &+ \begin{bmatrix} S^{\mathrm{P}}_{(1,1),(1,1)} & \cdots & S^{\mathrm{P}}_{(1,1),(M,N)} & S^{\mathrm{P}}_{(1,1),1\mathrm{e}} & \cdots & S^{\mathrm{P}}_{(1,1),T\mathrm{e}} \\ \vdots & & \vdots & \vdots & & \vdots \\ S^{\mathrm{P}}_{(M,N),(1,1)} & \cdots & S^{\mathrm{P}}_{(M,N),(M,N)} & S^{\mathrm{P}}_{(M,N),1\mathrm{e}} & \cdots & S^{\mathrm{P}}_{(M,N),T\mathrm{e}} \\ S^{\mathrm{P}}_{1\mathrm{e},(1,1)} & \cdots & S^{\mathrm{P}}_{1\mathrm{e},(M,N)} & S^{\mathrm{P}}_{1\mathrm{e},1\mathrm{e}} & \cdots & S^{\mathrm{P}}_{1\mathrm{e},T\mathrm{e}} \\ \vdots & & \vdots & \vdots & & \vdots \\ S^{\mathrm{P}}_{T\mathrm{e},(1,1)} & \cdots & S^{\mathrm{P}}_{T\mathrm{e},(M,N)} & S^{\mathrm{P}}_{T\mathrm{e},1\mathrm{e}} & \cdots & S^{\mathrm{P}}_{T\mathrm{e},T\mathrm{e}} \end{bmatrix} \Bigg\} \begin{bmatrix} a^{\mathrm{R}}_{(1,1)} \\ \vdots \\ a^{\mathrm{R}}_{(M,N)} \\ a^{\mathrm{R}}_{1\mathrm{e}} \\ \vdots \\ a^{\mathrm{R}}_{T\mathrm{e}} \end{bmatrix}. \end{aligned} \tag{10}$$

$$\begin{aligned} \boldsymbol{S}^{\mathrm{C}} = &\begin{bmatrix} S^{\mathrm{R}}_{(1,1),(1,1)} & \cdots & S^{\mathrm{R}}_{(1,1),(M,N)} \\ \vdots & & \vdots \\ S^{\mathrm{R}}_{(M,N),(1,1)} & \cdots & S^{\mathrm{R}}_{(M,N),(M,N)} \end{bmatrix} - \begin{bmatrix} S^{\mathrm{R}}_{(1,1),1\mathrm{e}} & \cdots & S^{\mathrm{R}}_{(1,1),T\mathrm{e}} \\ \vdots & & \vdots \\ S^{\mathrm{R}}_{(M,N),1\mathrm{e}} & \cdots & S^{\mathrm{R}}_{(M,N),T\mathrm{e}} \end{bmatrix} \begin{bmatrix} S^{\mathrm{R}}_{1\mathrm{e},1\mathrm{e}} - 1/S^{\mathrm{E}}_{1} & \cdots & S^{\mathrm{R}}_{1\mathrm{e},T\mathrm{e}} \\ \vdots & & \vdots \\ S^{\mathrm{R}}_{T\mathrm{e},1\mathrm{e}} & \cdots & S^{\mathrm{R}}_{T\mathrm{e},T\mathrm{e}} - 1/S^{\mathrm{E}}_{T} \end{bmatrix}^{-1} \\ &\cdot \begin{bmatrix} S^{\mathrm{R}}_{1\mathrm{e},(1,1)} & \cdots & S^{\mathrm{R}}_{1\mathrm{e},(M,N)} \\ \vdots & & \vdots \\ S^{\mathrm{R}}_{T\mathrm{e},(1,1)} & \cdots & S^{\mathrm{R}}_{T\mathrm{e},(M,N)} \end{bmatrix}. \end{aligned} \tag{11}$$

Thus, the procedure for designing the proposed PCN can be summarized as follows:

Step 1: Attain the scattering matrix $\boldsymbol{S}^{\mathrm{A}}$ of the upper original coupled antenna array.

Step 2: Add the coupling networks between the feeding lines of the array, reserve connecting ports for parasitic elements, and then obtain the scattering matrix $\boldsymbol{S}^{\mathrm{P}}$ of the lower part.

Step 3: Cascade $\boldsymbol{S}^{\mathrm{A}}$ with $\boldsymbol{S}^{\mathrm{P}}$ to obtain the scattering matrix $\boldsymbol{S}^{\mathrm{R}}$ of the composite network.

Step 4: Through the scattering relationship between parasitic ports and elements, the ultimate

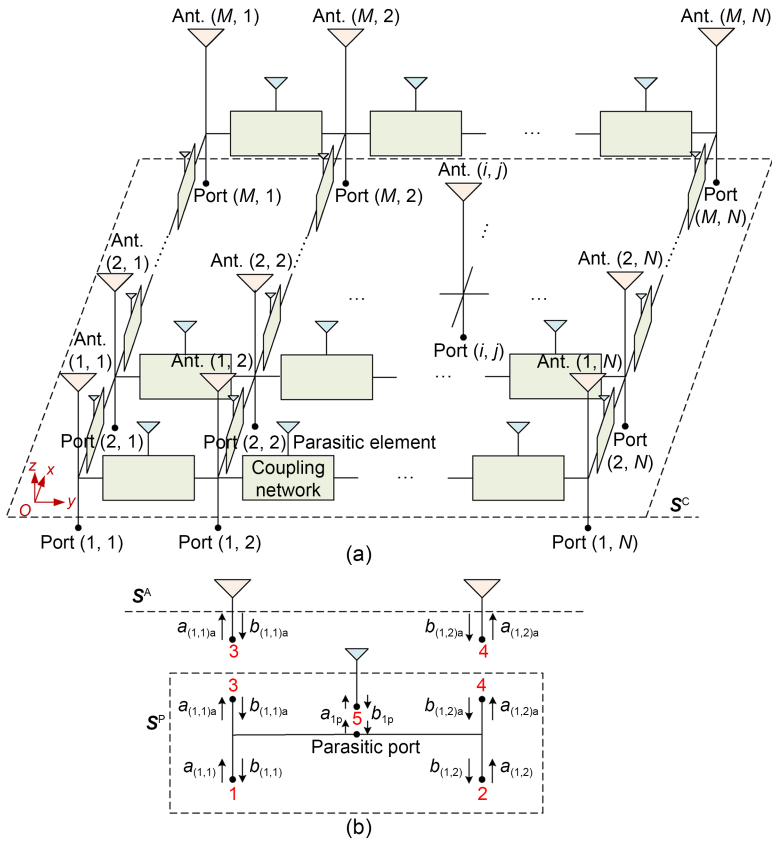

Fig. 2 Equivalent network model of an (M×N)-element antenna array loaded with parasitic coupling network (PCN): (a) overall construction; (b) network analysis process (subscript "p" refers to the parasitic port)

scattering matrix $\boldsymbol{S}^{\mathrm{C}}$ of the antenna array can be obtained.

Step 5: Estimate whether $\boldsymbol{S}^{\mathrm{C}}$ is congruent with the mutual coupling utilization condition; if not, return to Step 2 or 4 to adjust the coupling network or parasitic element.

3 Applications in wideband multielement microstrip antenna arrays

3.1 Dual-layer coupled microstrip antenna

Fig. 3 displays the geometry of the dual-layer coupled microstrip antenna, also known as a stacked microstrip antenna, which is a typical traditional and unbalanced-excitation wideband antenna and is selected as the array element in the design of the PCN. The element consists of two patches, one feeding line, three substrates, and the ground plane. The upper and lower patches, possessing the same size of l_{p}×w_{p}, are printed on the upper layers of the substrates with a relative

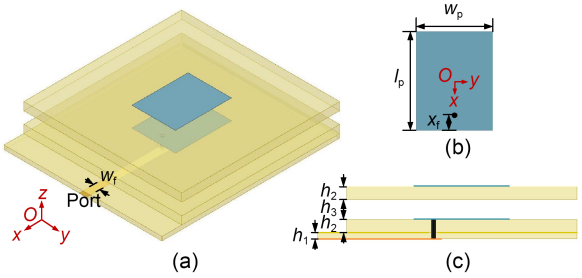

Fig. 3 Configuration of the unbalanced-excitation dual-layer coupled microstrip antenna: (a) overall view; (b) single patch; (c) side view

permittivity of 4.3, a loss tangent of 0.02, and a thickness of h_2, separated by an air gap with a height of h_3. Also, the lower patch is fed via a probe with a 0.8-mm diameter, which is connected to the feeding line with a width of w_{f} on the bottom layer of the lower substrate with a thickness of h_1, through a hole on the ground plane, and located at x_{f}-distance away from the short edge of the patch. The concrete dimensions of the antenna are listed in Table 1.

Table 1 Concrete dimensions of the dual-layer coupled microstrip antenna and the PCNs (unit: mm)

Parameter	Value	Parameter	Value	Parameter	Value	Parameter	Value	Parameter	Value
l_p	14.2	l_{h1}	4.7	w_{h1}	1.5	l_{e1}	8.6	w_{e1}	1.5
w_p	11	l_{h2}	3	w_{h2}	4	l_{e2}	9	w_{e2}	4
x_f	2.2	l_{h3}	21	w_{h3}	0.6	l_{e3}	26	w_{e3}	0.6
h_1	1	l_{h4}	9	w_{h4}	5	l_{e4}	13	w_{e4}	6.6
h_2	2	l_{h5}	6	w_{h5}	5.2	l_{e5}	5.4	w_{e5}	5.2
h_3	3	l_{h6}	3	w_{h6}	1	l_{e6}	3	w_{e6}	1
w_f	1.9	l_{h7}	4	w_{h7}	2	l_{e7}	4	w_{e7}	2

Fig. 4 plots the reflection coefficient and gain of the single dual-layer coupled antenna; the antenna operates in a broad band from 4.28 to 5.58 GHz, with the relative bandwidth attaining 26.4%. Meanwhile, the gains in the working band are all over 6.1 dBi and the maximum gain is 7.2 dBi at 5.46 GHz. However, when the antenna elements are compactly arranged in an array, the mutual coupling may deteriorate the characteristics. Thus, to intentionally use the coupling, a PCN is inserted between feeding lines to improve the array performance.

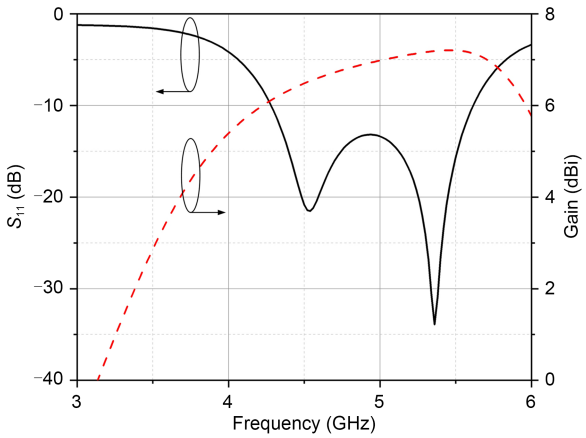

Fig. 4 The reflection coefficient and gain of the single dual-layer coupled microstrip antenna

3.2 PCN for two-element arrays

First, a two-element 1×2 coupled antenna array is employed for PCN design. To simplify the expression, the ports are denoted as port 1 and port 2. As the number of array elements becomes 2, Eq. (3) and inequality (5) can be respectively simplified to

$$S_{11\text{active}} = S_{11} + S_{21}, \tag{12}$$

$$\pi - \arccos\left(\frac{|S_{21}|}{2|S_{11}|}\right) \le \Delta\varphi \le \pi + \arccos\left(\frac{|S_{21}|}{2|S_{11}|}\right), \tag{13}$$

where the constitutive condition is $|S_{21}| \le 2|S_{11}|$. According to the constraint in inequality (13), it is easy to judge in which band the mutual coupling is available to improve the array performance. Take the coupled H-plane antenna array as an example. The edge-to-edge distance of the elements is only 5 mm ($0.083\lambda_0$; λ_0 is the wavelength corresponding to the center frequency of the working band) and the center-to-center spacing is $0.27\lambda_0$. The antenna array is fabricated and its *S*-parameters are measured via a vector network analyzer. The simulated and measured *S*-parameters and phases of the array are plotted in Fig. 5. The simulated working band with only port 1 excited is 4.44–5.68 GHz (24.5%), while the measured one is 4.46–5.64 GHz (23.4%). In light of the calculated phase differences and boundary values exhibited in Fig. 5b, it is obvious that mutual coupling in the simulated bands of 3.00–4.62 GHz and 4.86–5.40 GHz can be used and the measured ones are 3.00–4.56 GHz and 4.90–5.40 GHz. It is worth mentioning that, although there is a relatively great disparity between the simulated and measured phase differences because of the measurement deviation and fabrication error, the curves both fall, as expected, within the boundaries. Therefore, when two ports are both excited, the simulated and measured bands of the ARC that are lower than −10 dB (voltage standing wave ratio (VSWR), <2) expand to 4.10–5.58 GHz (30.6%) and 4.12–5.56 GHz (29.8%), respectively. It is also noted that the missing data of the boundary values result from failing to satisfy the constitutive condition.

However, through loading the PCN, the operating band can be further widened. Following the design process of the PCN implementation, the scattering matrix

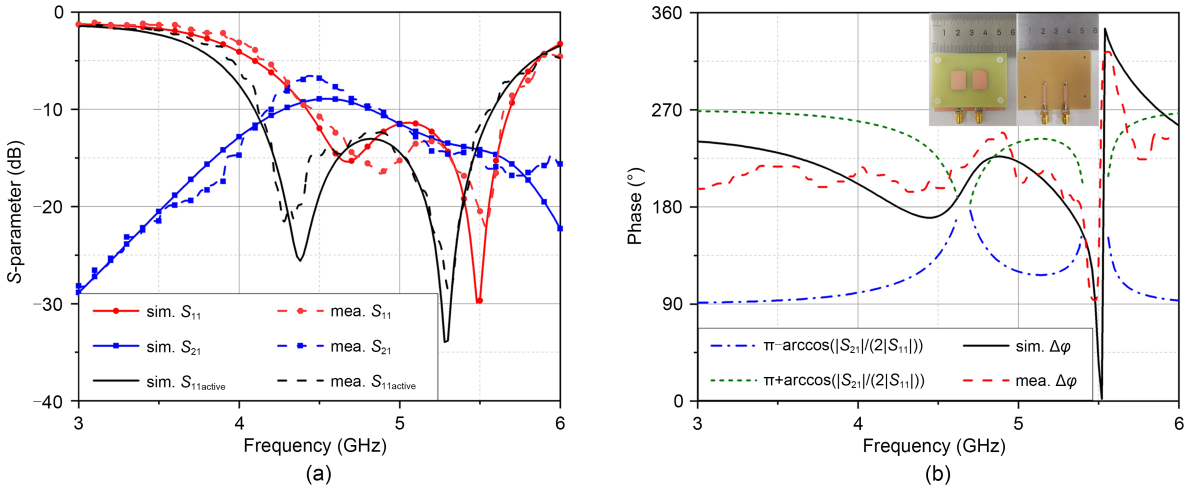

Fig. 5 ***S*-parameters and phase differences of the original H-plane antenna array: (a) *S*-parameters; (b) phase differences and the fabricated array**

of the original antenna array is obtained. Here, an out-of-band frequency of 4 GHz is selected as a typical object.

$$\boldsymbol{S}^{\mathrm{A}}=\begin{bmatrix}0.72\mathrm{e}^{\mathrm{j}\cdot 1.45} & 0.21\mathrm{e}^{\mathrm{j}\cdot(-1.29)}\\ 0.21\mathrm{e}^{\mathrm{j}\cdot(-1.29)} & 0.72\mathrm{e}^{\mathrm{j}\cdot 1.45}\end{bmatrix}. \tag{14}$$

As Fig. 6 shows, a shorted stepped microstrip parasitic element is inserted between two patches on the middle substrate, which is linked to the coupling network via a metal probe, then $S_1^{\mathrm{E}}=0.96\mathrm{e}^{\mathrm{j}\cdot(-0.31)}$. The coupling network consists of two shorted and one open T-stubs, which are equivalent to transmission lines (Sui and Wu, 2017), enabling the transmission magnitude and phase of the five-port network, calculated as Eq. (15) (at the bottom of this page), to adjust to those of the original array for better characteristics. The detailed dimensions of the PCN are listed in Table 1.

Therefore, the ultimate scattering matrix of the antenna array with the PCN can be calculated according to Eq. (11) as

$$\boldsymbol{S}^{\mathrm{C}}=\begin{bmatrix}0.43\mathrm{e}^{\mathrm{j}\cdot 1.34} & 0.32\mathrm{e}^{\mathrm{j}\cdot(-1.12)}\\ 0.32\mathrm{e}^{\mathrm{j}\cdot(-1.12)} & 0.43\mathrm{e}^{\mathrm{j}\cdot 1.34}\end{bmatrix}. \tag{16}$$

Then, the ARC at 4 GHz is further calculated as −11.32 dB, and the phase difference is 141.2°, which is within the boundary values (111.9°, 248.1°), indicating that the mutual coupling is successfully used. If not, the parasitic element or coupling network can be tuned to achieve the demanded scattering matrices.

To better understand how the geometry of the PCN affects the ARC, four main structure parameters are chosen, which are presented in Fig. 7. For the parasitic element between the lower patches, when its length l_{h2} is shorter than 5 mm, the ARC bandwidth in Fig. 7a changes a little, and only the high band enlarges with the length increasing. When it turns longer, the low band is narrowed down. While for the coupling network, its position in the feeding network can greatly influence the ARC, which is plotted in Fig. 7b. In detail, the longer the length l_{h4} is, the better the impedance matching can be. Meanwhile, the length and position of the T-stubs of the coupling network can exert influence on the ARC. In Fig. 7c, when the length l_{h6} increases, the high band is slightly narrowed. As shown in Fig. 7d, when the two branches are remotely separated, which indicates that the width w_{h4} has increased,

$$\boldsymbol{S}^{\mathrm{P}}=\begin{bmatrix}0.40\mathrm{e}^{\mathrm{j}\cdot(-0.93)} & 0.02\mathrm{e}^{\mathrm{j}\cdot 1.68} & 0.85\mathrm{e}^{\mathrm{j}\cdot(-2.96)} & 0.03\mathrm{e}^{\mathrm{j}\cdot 1.21} & 0.17\mathrm{e}^{\mathrm{j}\cdot 3.02}\\ 0.02\mathrm{e}^{\mathrm{j}\cdot 1.68} & 0.40\mathrm{e}^{\mathrm{j}\cdot(-0.93)} & 0.03\mathrm{e}^{\mathrm{j}\cdot 1.21} & 0.85\mathrm{e}^{\mathrm{j}\cdot(-2.96)} & 0.17\mathrm{e}^{\mathrm{j}\cdot 3.02}\\ 0.85\mathrm{e}^{\mathrm{j}\cdot(-2.96)} & 0.03\mathrm{e}^{\mathrm{j}\cdot 1.21} & 0.40\mathrm{e}^{\mathrm{j}\cdot(-1.73)} & 0.02\mathrm{e}^{\mathrm{j}\cdot 0.97} & 0.18\mathrm{e}^{\mathrm{j}\cdot 2.77}\\ 0.03\mathrm{e}^{\mathrm{j}\cdot 1.21} & 0.85\mathrm{e}^{\mathrm{j}\cdot(-2.96)} & 0.02\mathrm{e}^{\mathrm{j}\cdot 0.97} & 0.40\mathrm{e}^{\mathrm{j}\cdot(-1.73)} & 0.18\mathrm{e}^{\mathrm{j}\cdot 2.77}\\ 0.17\mathrm{e}^{\mathrm{j}\cdot 3.02} & 0.17\mathrm{e}^{\mathrm{j}\cdot 3.02} & 0.18\mathrm{e}^{\mathrm{j}\cdot 2.77} & 0.18\mathrm{e}^{\mathrm{j}\cdot 2.77} & 0.87\mathrm{e}^{\mathrm{j}\cdot(-1.08)}\end{bmatrix}. \tag{15}$$

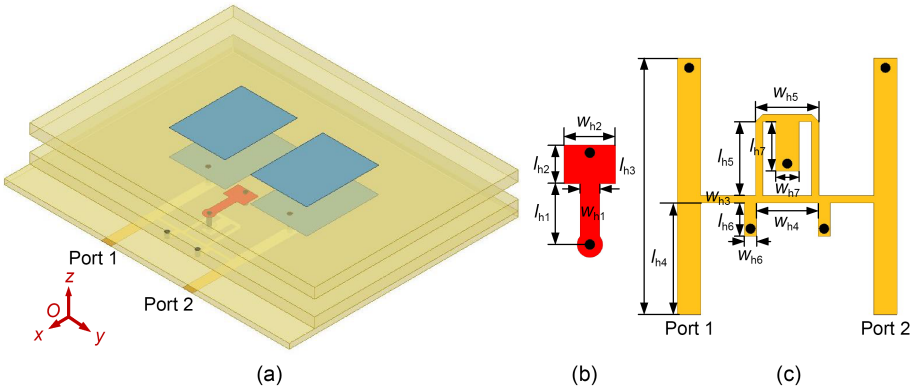

Fig. 6 PCN implementation for the two-element H-plane antenna array: (a) overall view; (b) parasitic element; (c) coupling network

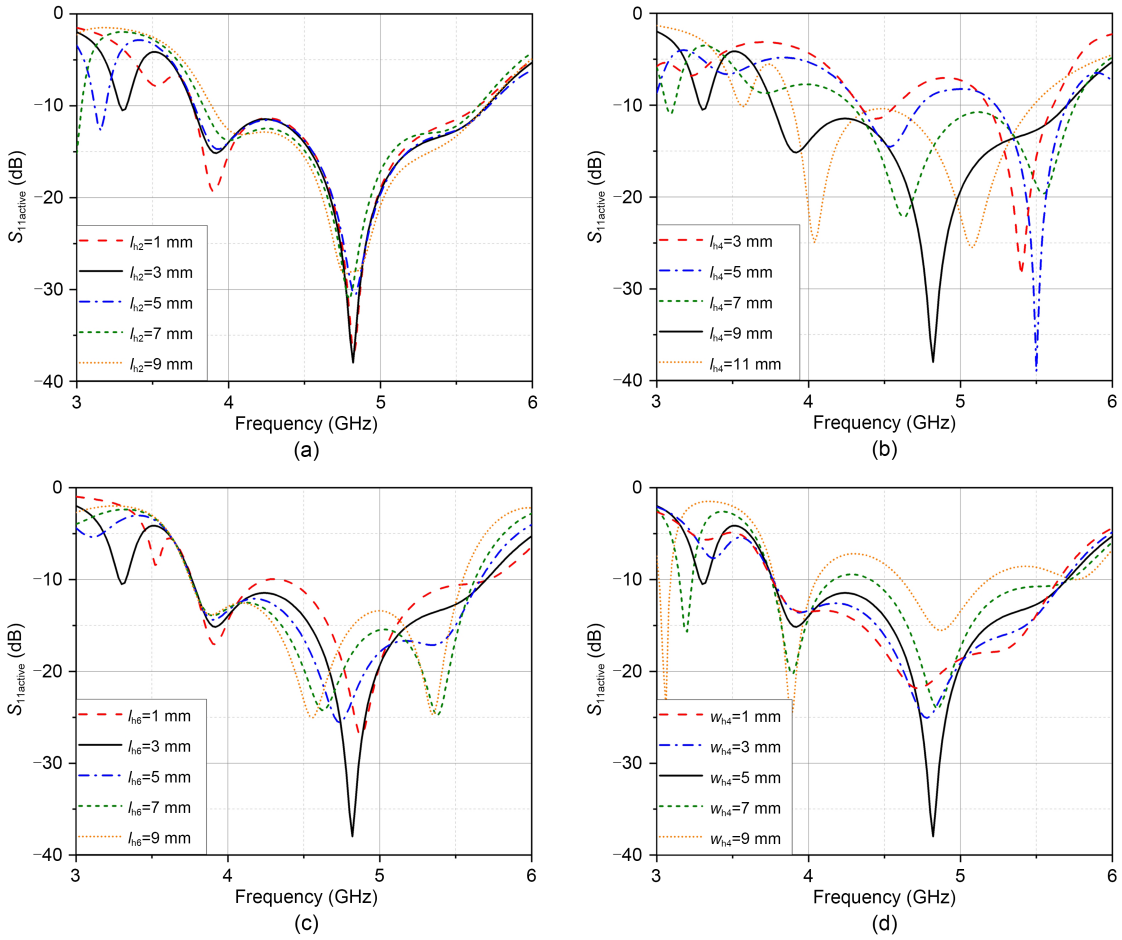

Fig. 7 $S_{11active}$ versus l_{h2} (a), l_{h4} (b), l_{h6} (c), and w_{h4} (d) of the H-plane antenna array with the PCN

the ARC becomes worse. Thus, the four parameters are determined as listed in Table 1.

Fig. 8 demonstrates the simulated and measured *S*-parameters and phase differences of the antenna array loading with the PCN. It is worth noting that the simulated results at 4 GHz are consistent with the calculated ones, verifying the correctness of the PCN implementation. Likewise, the mutual coupling in the band of 3.50–5.06 GHz can be used for both the simulated and measured bandwidth enhancements. Thus, the

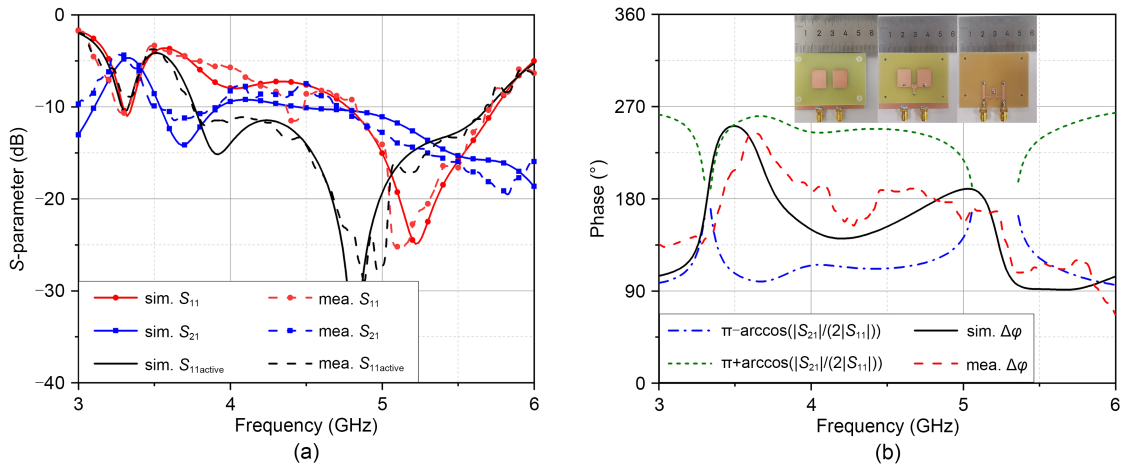

Fig. 8 *S*-parameters and phase differences of the H-plane antenna array with the PCN: (a) *S*-parameters; (b) phase differences and the fabricated array

simulated and measured bandwidths of the ARC are 3.78–5.70 GHz (40.5%) and 3.76–5.68 GHz (40.7%), respectively, which are 9.9% and 10.9% wider than those of the original array.

The simulated and measured normalized radiation patterns and gains of the antenna array without or with the PCN are presented in Figs. 9 and 10a, respectively. The measurement and simulation results coincide well with each other. It is observed that the additional PCN has little impact on the radiation characteristics, as both the radiation pattern and gain diminutively vary in the operating band, where the gains of the antenna array with the network are all over 5.7 dBi. All the cross-polarization levels in the E-plane are lower than −35 dB, which are not displayed in Fig. 9. However, those in the H-plane at 4.1 GHz and 5.6 GHz are lower than −20 dB and −23 dB, respectively, and vary little after loading the PCN. Meanwhile, the radiation efficiencies of the two-element antenna array without or with the PCN are plotted in Fig. 10b, which further reveals that the introduced PCN has little influence on the radiation. The simulated and measured radiation efficiencies of the array with the PCN are over 62.4% and 64.4% in the operating band, and can reach a maximum of 86.2% and 83.4%, respectively. It is noted that the gains and radiation efficiencies both have roll-off after loading the PCN, but they occur mainly in the low band. The reason is that a filtering response is generated due to the coupling effect, which can also be observed in Fig. 8a. However, this response has little influence on the array performance within the operating band. Different from the parasitic decoupling, which has an influence on the radiation performance, the introduced parasitic element in the PCN, which is employed to guide the coupling currents between the array elements and the coupling network, brings about little change; thus, it mainly plays a role as a matching element.

One key factor of the multielement antenna system, the envelope correlation coefficient (ECC), is plotted in Fig. 11 to evaluate the PCN performance. Often, the larger the ECC is, the stronger the relationship between the array elements will be. It is evident that, at around 4 GHz, the ECC of the H-plane antenna array with the PCN is larger than that of the array without the PCN, which indicates that the PCN helps enhance the correlation between elements and widen the ARC bandwidth.

E-field and current distributions of the antenna array with the PCN are further presented in Fig. 12. From the E-field distribution, it is apparent that the array is capable of radiating forward at 4.1 GHz and 5.6 GHz, as is the current distribution, which also verifies that the upper and lower patches cooperate to obtain an excellent radiation performance.

Following the design procedure of the PCN for the H-plane antenna array, the procedure for a 2×1 E-plane array is presented in Fig. 13. The edge-to-edge distance of two elements is still 5 mm, leading the center-to-center one to be $0.32\lambda_0$. Since the array is asymmetric along the y axis, one meander line is augmented to the parasitic element to ensure the symmetric arrangement of the coupling network. The

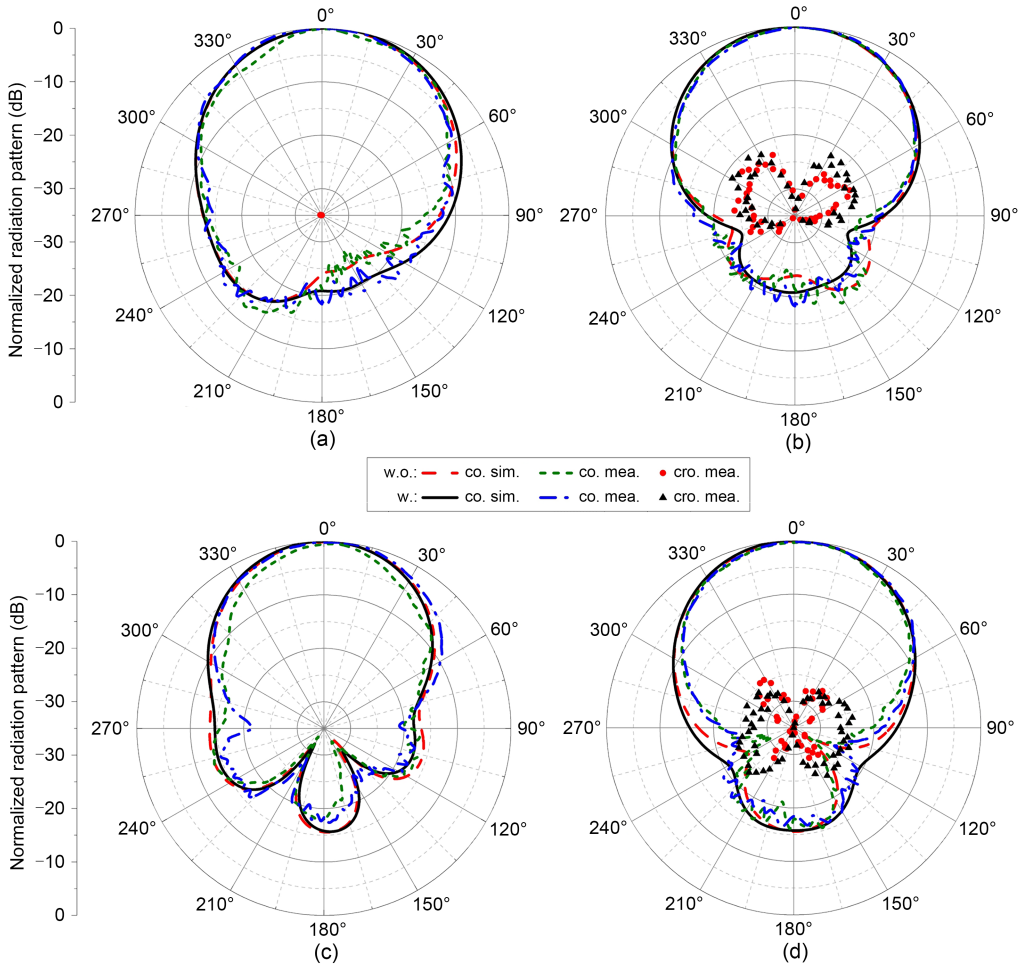

Fig. 9 Simulated and measured normalized radiation patterns of the two-element H-plane antenna array without (w.o.) or with (w.) the PCN: E-plane (a) and H-plane (b) at 4.1 GHz; E-plane (c) and H-plane (d) at 5.6 GHz (Cro. represents cross-polarization)

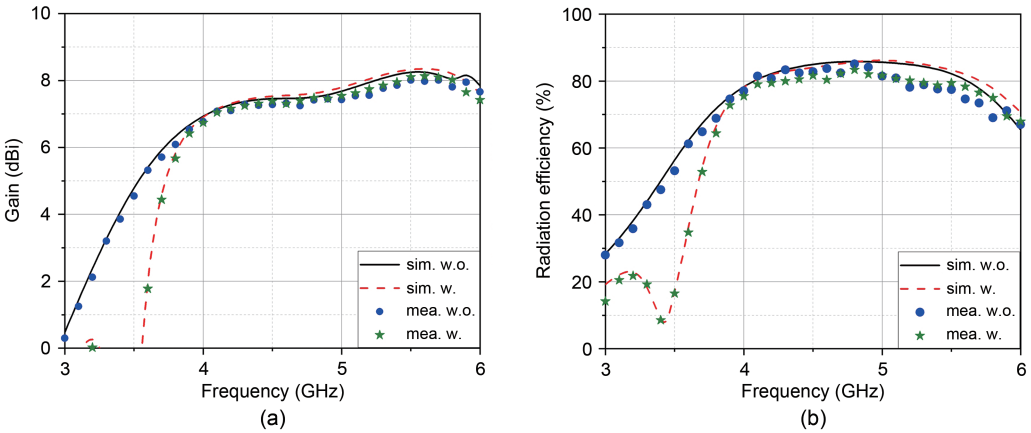

Fig. 10 Simulated and measured gains (a) and radiation efficiencies (b) of the two-element H-plane antenna array without or with the PCN

dimensions are listed in Table 1. Both of the E-plane antenna arrays (with/without PCN) are simulated, fabricated, and measured. Fig. 14 illustrates that the mutual coupling in the band of missing boundary

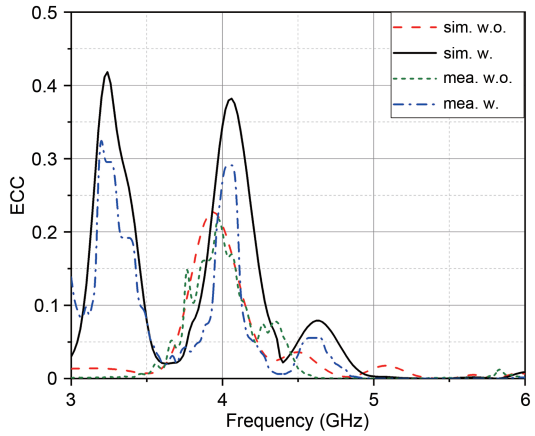

Fig. 11 Simulated and measured envelope correlation coefficients (ECCs) of the two-element H-plane antenna array without or with the PCN

data between the elements deteriorates the array performance; although that in the band of 3.00–4.30 GHz can be used, the ARC is immensely decreased. However, from Fig. 15, the proposed PCN not only relieves the influence of the mutual coupling in the band of missing boundary data, but also leverages that in the band of 3.00–4.68 GHz to expand the measured operating ARC band from 4.00–4.40 GHz (9.5%) to 3.80–5.72 GHz (40.3%), which is huge progress for a 30.8% bandwidth increment. Based on the above results, it can be concluded that the results imply the effectiveness of using the PCN for the performance improvement of arrays arranged along the H-plane and E-plane.

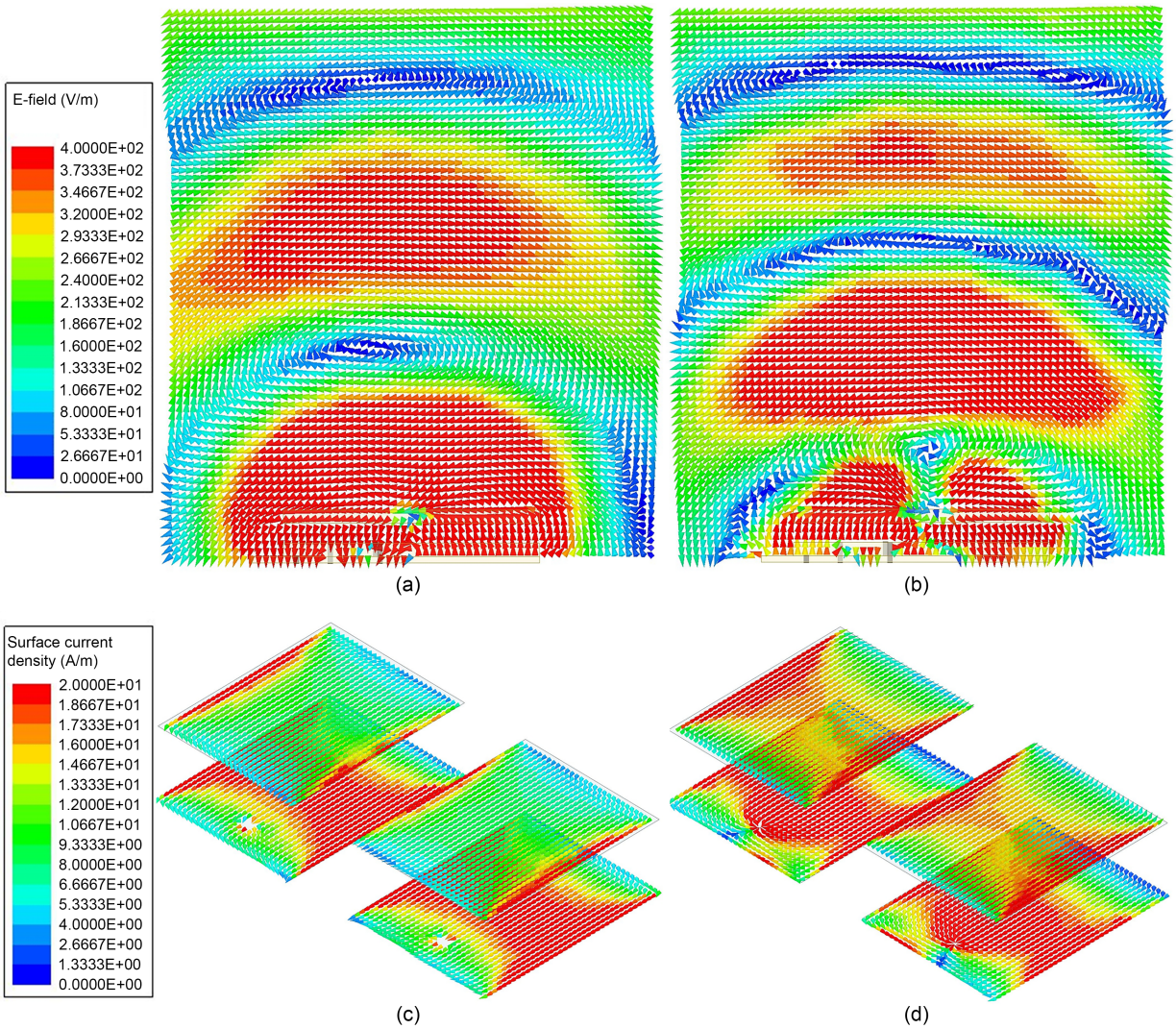

Fig. 12 E-field and current distributions of the two-element H-plane antenna array with the PCN: E-field distribution at 4.1 GHz (a) and 5.6 GHz (b); current distribution at 4.1 GHz (c) and 5.6 GHz (d)

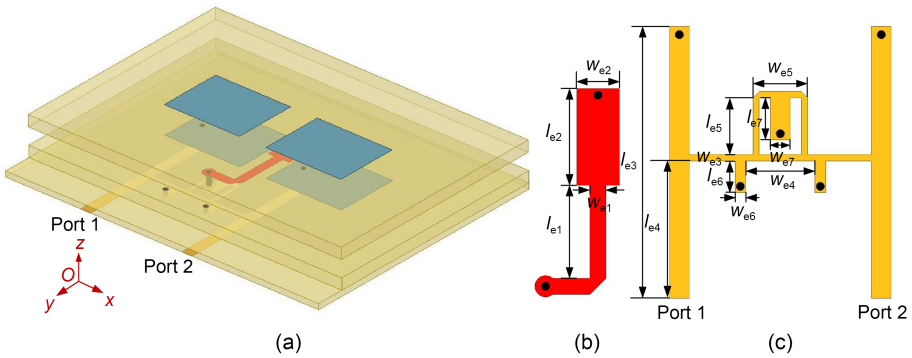

Fig. 13 PCN implementation for the two-element E-plane antenna array: (a) overall view; (b) parasitic element; (c) coupling network

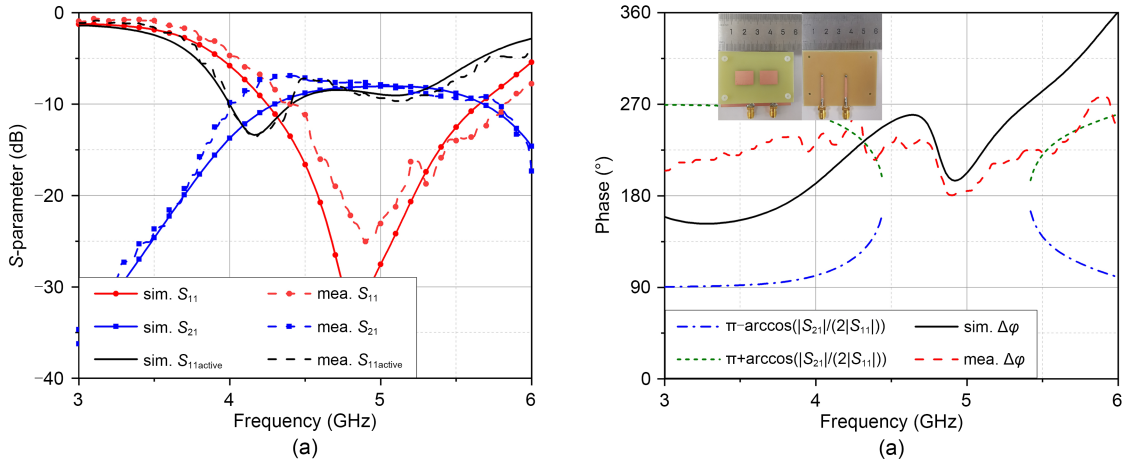

Fig. 14 *S*-parameters and phase differences of the original E-plane antenna array: (a) *S*-parameters; (b) phase differences and the fabricated array

3.3 PCN for multielement arrays

Subsequently, PCNs are finely adjusted to increase the bandwidths of three- and five-element H-plane antenna arrays (see supplementary materials, Sections 1 and 2), indicating that the proposed method is efficient in extending the ARC bandwidth of multielement linear arrays.

Since the effectiveness of the PCN for both the H-plane and E-plane antenna arrays has been previously verified, its application in a two-dimensional array is further briefly investigated here. Fig. 16 depicts the fabricated prototype of the proposed PCN for an 8×2 antenna array, which is extended to two elements along the H-plane based on a linear eight-element E-plane array; thus, it remains symmetric along the *y* axis and relatively symmetric along the *x* axis. The geometry remains in the same configuration with several parameters precisely tuned to fully use mutual coupling. It is noteworthy that the edge-to-edge spacing of both E-plane and H-plane elements is still 5 mm, and the PCN is mainly based on that for the two-element E-plane antenna array in Fig. 13, while that for the H-plane array, shown in Fig. 6, is bent to match the overall structure. Since the antenna array has 16 ports, to simplify the expression of the *S*-parameters, the 16 ports are denoted as port 1 to port 16, and ports 1, 3, 5, and 7 are especially studied.

Fig. 17 delivers the ARCs of the 8×2 antenna array without or with the PCN and coupling utilization evaluations of the latter. For the original antenna array, as displayed in Fig. 17a, the ARCs apparently deteriorate due to the strong mutual coupling between array elements and no effective coupling manipulation method. The middle element suffers from the largest influence; thus, the ARC at port 5 is around −5 dB

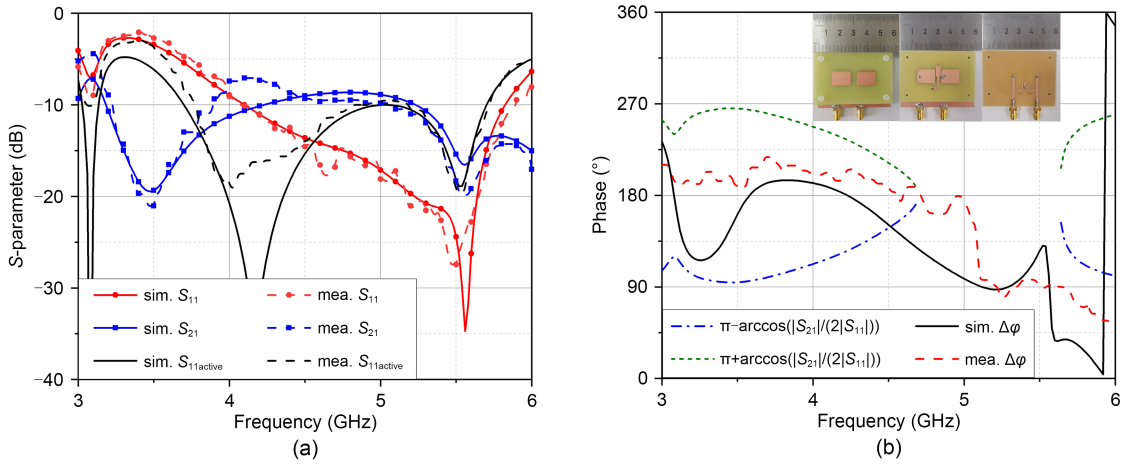

Fig. 15 ***S*-parameters and phase differences of the E-plane antenna array with the PCN: (a) *S*-parameters; (b) phase differences and the fabricated array**

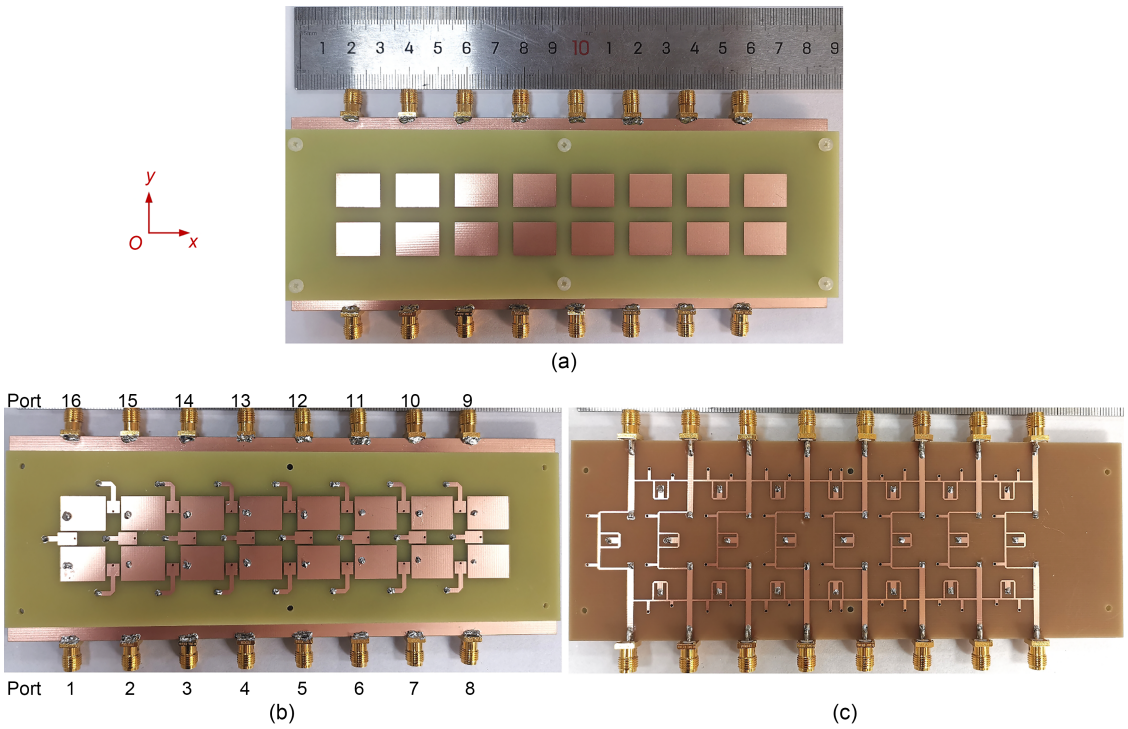

Fig. 16 Prototype of the proposed PCN for the two-dimensional 8×2 antenna array: (a) upper patches; (b) lower patches and parasitic elements; (c) coupling network

across almost the whole band. However, by using the coupling network to manipulate the mutual coupling between array elements, the ARCs are all improved. Figs. 17c–17f show that, for ports 1, 3, 5, and 7, the simulated bands where the phase differences satisfy the mutual coupling utilization conditions are, respectively, 3.00–4.02 and 4.28–5.04, 3.56–4.42, 3.00–4.54, and 3.00–4.94 GHz, while the measured ones are, respectively, 3.00–4.02 and 4.30–5.04, 3.00–4.56, 3.00–4.78, and 3.00–4.80 GHz. Then, the corresponding simulated ARC bands are expanded to 3.40–6.62, 3.54–5.96, 3.72–5.98, and 3.44–7.00 GHz, while the measured ones are 3.66–6.68, 3.40–6.08, 3.50–5.92, and 3.54–6.16 GHz. Thus, the simulated and measured shared operating bands are 3.72–5.96 GHz (46.3%) and 3.66–5.92 GHz (47.2%), respectively. Fig. 18a plots

the gains of the 8×2 antenna array without or with the PCN, which indicates that the simulated and measured gains of the antenna array with the PCN vary between 13.1 and 16.1 dBi and 12.7 and 16.0 dBi, respectively, and are higher than those of the array without the PCN at most frequencies. Moreover, the higher radiation efficiencies in Fig. 18b demonstrate that the antenna array with the PCN exhibits a better radiation performance, since in the operating band, the simulated and measured radiation efficiencies are all over 62.1% and 60.3%, while the maximum ones reach 94.2% and 88.8%, respectively.

The scanning characteristics are also studied in this planar case. The ARCs and mutual coupling utilization condition can be obtained according to Eq. (4) and inequality (5). Figs. 19 and 20, respectively, demonstrate the scanning ARCs and phase differences of the 8×2 antenna array with the PCN. To simplify the analysis, only the relative characteristics are delivered when scanning in the $+x$ and $+y$ directions. From

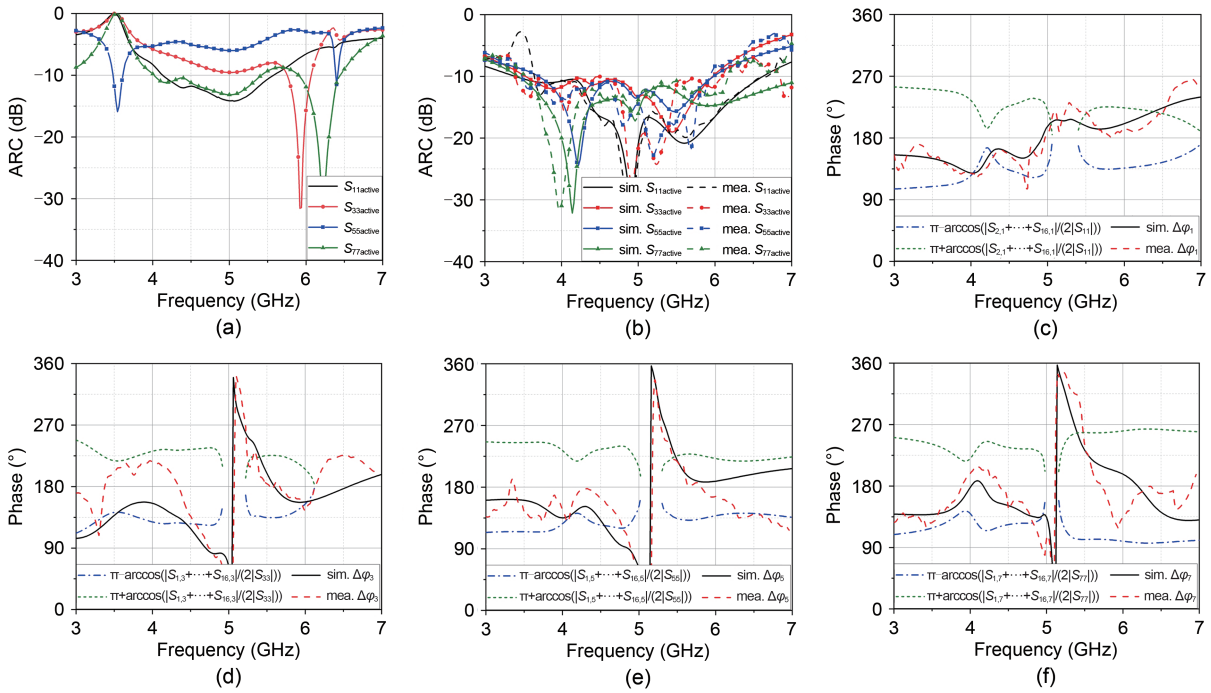

Fig. 17 ARCs and phase differences of the 8×2 antenna array without or with the PCN: (a) ARC of the array without the PCN; (b) ARC of the array with the PCN; (c) phase difference of port 1; (d) phase difference of port 3; (e) phase difference of port 5; (f) phase difference of port 7

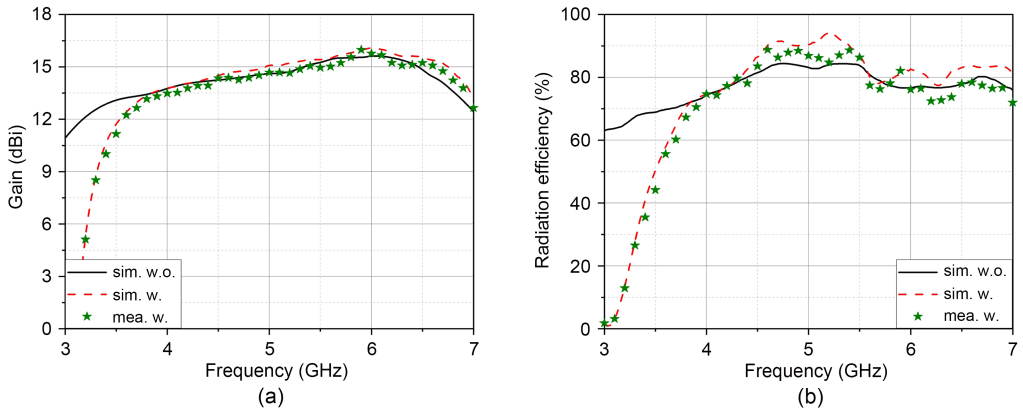

Fig. 18 Simulated and measured gains (a) and radiation efficiencies (b) of the 8×2 antenna array without or with the PCN

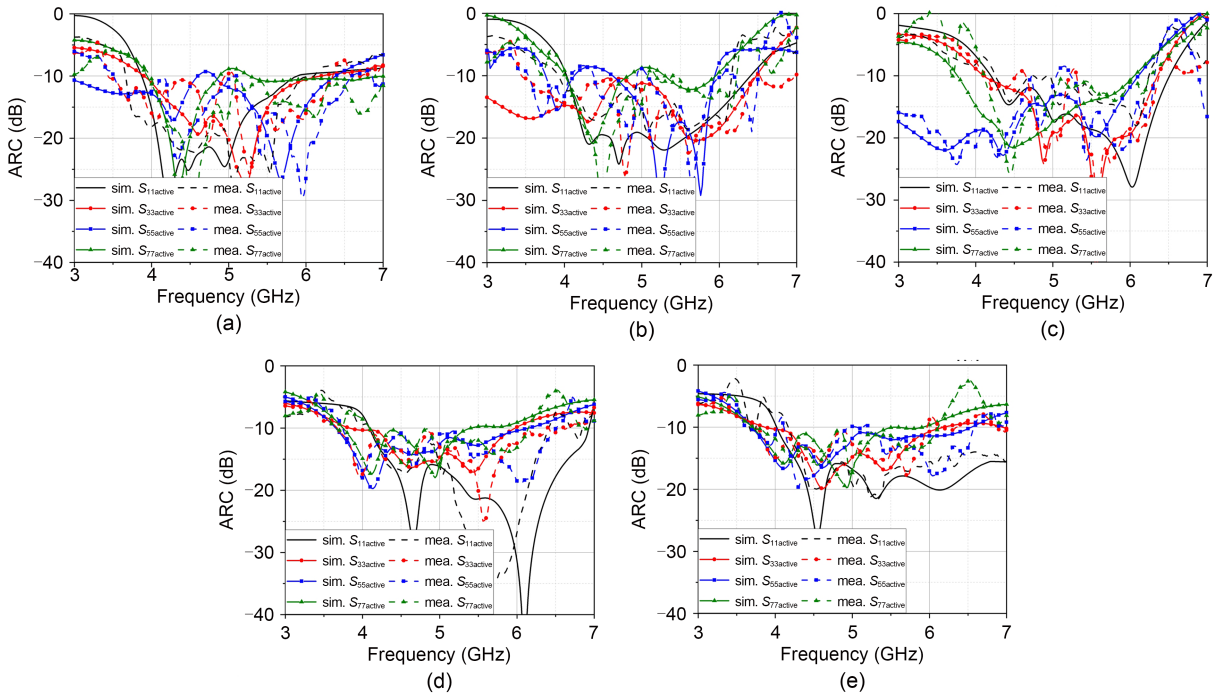

Fig. 19 Scanning ARCs of the 8×2 antenna array with the PCN: 30° (a), 45° (b), and 60° (c) for E-plane scanning; 30° (d) and 45° (e) for H-plane scanning

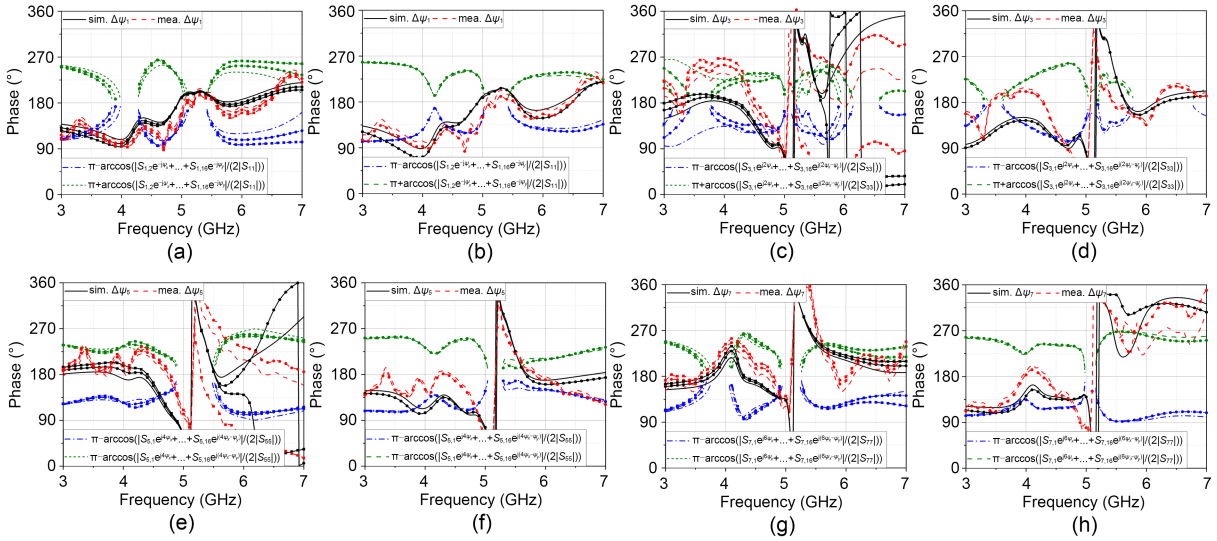

Fig. 20 Scanning phase differences of the 8×2 antenna array with the PCN: port 1 (a), port 3 (c), port 5 (e), and port 7 (g) for E-plane scanning (line: 30°, line+circle: 45°, line+square: 60°); port 1 (b), port 3 (d), port 5 (f), and port 7 (h) for H-plane scanning (line: 30°, line+circle: 45°)

Figs. 20b, 20d, 20f, and 20h, it is obvious that the mutual coupling utilization conditions demonstrate almost no change with the varying H-plane scanning angles, as do the simulated and measured phase differences; the coupling can thus still be used for the scanning antenna array. Therefore, when the array scans to 30° and 45° in the H-plane, the measured operating bands of active VSWRs lower than 2.3 are 3.94–6.22 GHz (44.9%) and 4.10–6.18 GHz (40.5%). For E-plane scanning, there are missing data about the mutual coupling utilization conditions, which have little impact on the ARC bandwidth.

Meanwhile, varying the scanning angle can create a huge effect on the phase difference, especially for the middle elements 3 and 5, as displayed in Figs. 20c and 20e. However, as the PCN is designed mainly for the bandwidth expansion of low bands, this part of the effect can be ignored. Thus, it is shown in Figs. 19a–19c that the measured operating bands of active VSWRs lower than 2.3 are 3.86–6.40 GHz (49.5%), 3.98–6.16 GHz (43.0%), and 4.08–6.30 GHz (42.8%), respectively, for scanning to 30°, 45°, and 60°, and the shared band is 4.08–6.16 GHz (40.6%). Above all, the shared ARC bandwidth for both H-plane and E-plane scanning is 40.2% (4.10–6.16 GHz).

Fig. 21 plots the normalized scanning radiation patterns at 4.5 and 5.5 GHz, which implies that the E-plane and H-plane scanning ranges can reach ±60° and ±45°, respectively. However, the E-plane patterns are asymmetric, since the antenna array is not symmetric along the E-plane, while the H-plane patterns have good symmetry. At 4.5 GHz, the simulated and measured gain variations are 1.4 and 1.3 dB for E-plane scanning respectively, and both 1.3 dB for H-plane scanning. At 5.5 GHz, the simulated and measured variations are 3.0 and 2.7 dB for E-plane scanning, and 0.4 and 0.5 dB for H-plane scanning. Therefore, the variations are all within 3 dB, indicating that the antenna array with the PCN has wide-angle scanning capability. The whole cross-polarization levels in the E-plane are lower than −55 dB; thus, the curves are not displayed in Figs. 21a or 21c. Those in the H-plane are lower than −15 dB, which is still within an acceptable level.

4 Conclusions

In this article, a new concept for using mutual coupling by introducing the PCN is proposed and applied to the unbalanced-excitation array and dual-layer coupled microstrip antenna array. The mutual coupling utilization condition is deduced according to the network model, as well as the PCN implementation in an (M×N)-element antenna array. Starting from its employment in the two-element H-plane coupled antenna array, the PCN is widely applied to the E-plane array, multielement one-dimensional arrays, and the two-dimensional array, step by step. Compared with those

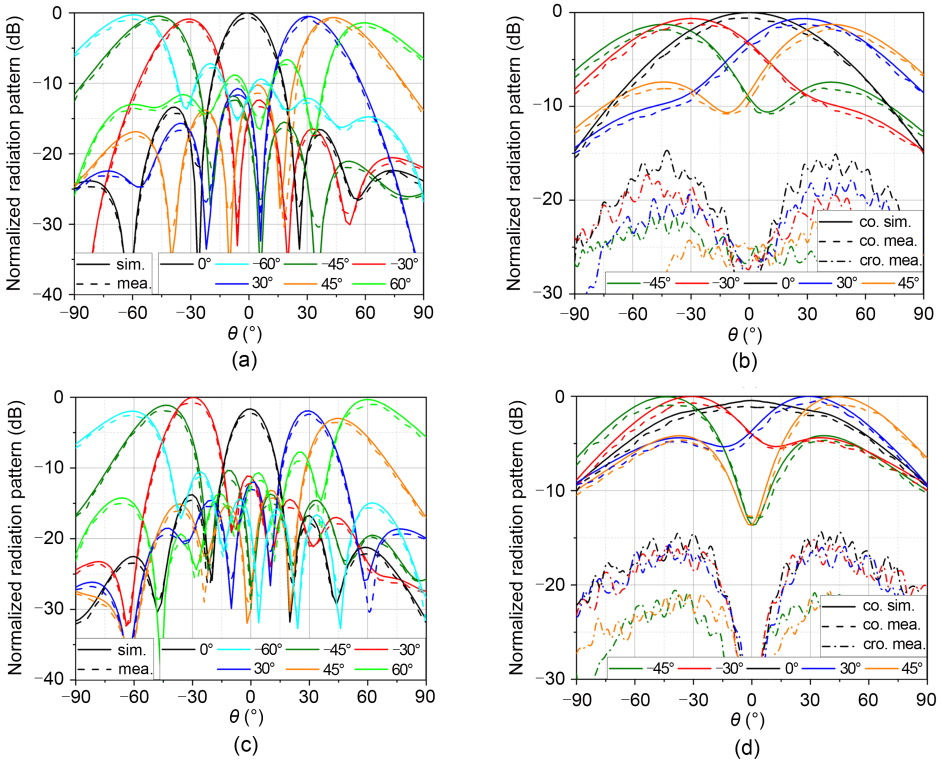

Fig. 21 Normalized scanning radiation patterns of the 8×2 antenna array with the PCN: 4.5 GHz (a) and 5.5 GHz (c) for E-plane radiation patterns; 4.5 GHz (b) and 5.5 GHz (d) for H-plane radiation patterns

without the PCN, the characteristics of these arrays are improved, including approximately 40% overlapped ARC bandwidths, normal radiation patterns, steady gains, and applicable scanning characteristics. The novel PCN illustrates its potential application in wideband unbalanced-excitation large-scale phased antenna arrays. However, only one antenna type is chosen to verify the effectiveness of the PCN concept; thus, future research can focus on PCN design for various kinds of antennas. In addition, the optimization algorithm can be employed to hasten PCN design.

Contributors

Xiaojun ZOU contributed to the idea, simulation, and measurement, and drafted the paper. Guangming WANG, Yawei WANG, and Binfeng ZONG contributed to the technical discussion and helped organize the paper. Wei SONG, Hang ZHU, Ming TAN, Xuguang XU, and Guoqin KANG contributed to the measurement and helped finalize the paper.

Conflict of interest

All the authors declare that they have no conflict of interest.

Data availability

The data that support the findings of this study are available from the corresponding author upon reasonable request.

References

Allen JL, Diamond BL, 1966. Mutual Coupling in Array Antennas. Technical Report No. 424 (ESD-TR-66-443), Lincoln Laboratory, MIT, Lexington, MA, USA.

Alwan EA, Sertel K, Volakis JL, 2012. A simple equivalent circuit model for ultrawideband coupled arrays. *IEEE Antenn Wirel Propag Lett*, 11:117-120. https://doi.org/10.1109/LAWP.2012.2184257

Bait-Suwailam MM, Boybay MS, Ramahi OM, 2010. Electromagnetic coupling reduction in high-profile monopole antennas using single-negative magnetic metamaterials for MIMO applications. *IEEE Trans Antenn Propag*, 58(9): 2894-2902. https://doi.org/10.1109/TAP.2010.2052560

Chen YK, Zhou WY, Yang SW, 2021. Design of a low-profile and low scattering wideband planar phased antenna array. *IEEE Trans Antenn Propag*, 69(12):8973-8978. https://doi.org/10.1109/TAP.2021.3097099

Ghadimi A, Nayyeri V, Khanjarian M, et al., 2020. A systematic approach for mutual coupling reduction between microstrip antennas using pixelization and binary optimization. *IEEE Antenn Wirel Propag Lett*, 19(12):2048-2052. https://doi.org/10.1109/LAWP.2020.3022000

Guo JY, Liu F, Jing GD, et al., 2020. Mutual coupling reduction of multiple antenna systems. *Front Inform Technol Electron Eng*, 21(3):366-376. https://doi.org/10.1631/FITEE.1900490

Holland SS, Vouvakis MN, 2012. The planar ultrawideband modular antenna (PUMA) array. *IEEE Trans Antenn Propag*, 60(1):130-140. https://doi.org/10.1109/TAP.2011.2167916

Kahn W, 1969. Active reflection coefficient and element efficiency in arbitrary antenna arrays. *IEEE Trans Antenn Propag*, 17(5):653-654. https://doi.org/10.1109/tap.1969.1139526

Kumar C, Pasha MI, Guha D, 2017. Defected ground structure integrated microstrip array antenna for improved radiation properties. *IEEE Antenn Wirel Propag Lett*, 16:310-312. https://doi.org/10.1109/LAWP.2016.2574638

Kumar P, Pathan S, Vincent S, et al., 2023. A compact quad-port UWB MIMO antenna with improved isolation using a novel mesh-like decoupling structure and unique DGS. *IEEE Trans Circ Syst II Exp Briefs*, 70(3):949-953. https://doi.org/10.1109/TCSII.2022.3220542

Lau BK, Andersen JB, 2012. Simple and efficient decoupling of compact arrays with parasitic scatterers. *IEEE Trans Antenn Propag*, 60(2):464-472. https://doi.org/10.1109/TAP.2011.2173440

Li M, Jiang LJ, Yeung KL, 2019. Novel and efficient parasitic decoupling network for closely coupled antennas. *IEEE Trans Antenn Propag*, 67(6):3574-3585. https://doi.org/10.1109/TAP.2019.2902656

Li M, Jiang LJ, Yeung KL, 2020. A general and systematic method to design neutralization lines for isolation enhancement in MIMO antenna arrays. *IEEE Trans Veh Technol*, 69(6): 6242-6253. https://doi.org/10.1109/TVT.2020.2984044

Li M, Zhang YJ, Wu D, et al., 2022a. Decoupling and matching network for dual-band MIMO antennas. *IEEE Trans Antenn Propag*, 70(3):1764-1775. https://doi.org/10.1109/TAP.2021.3118791

Li M, Zhang YJ, Jiang F, et al., 2022b. Improvement for MIMO systems by increasing antenna isolation and shaping radiation pattern using hybrid network. *IEEE Trans Ind Electron*, 69(12):13891-13901. https://doi.org/10.1109/TIE.2021.3128914

Li WT, Tu HC, He YJ, et al., 2023. A novel wideband tightly coupled dual-polarized reflectarray antenna. *IEEE Trans Antenn Propag*, 71(6):5422-5427. https://doi.org/10.1109/TAP.2023.3262969

Liu F, Guo JY, Zhao LY, et al., 2020. Dual-band metasurface-based decoupling method for two closely packed dual-band antennas. *IEEE Trans Antenn Propag*, 68(1):552-557. https://doi.org/10.1109/TAP.2019.2940316

Munk B, Taylor R, Durharn T, et al., 2003. A low-profile broadband phased array antenna. Proc IEEE Antennas and Propagation Society Int Symp, p.448-451. https://doi.org/10.1109/APS.2003.1219272

Qu SW, Chan CH, Xia MY, et al., 2013. High-efficiency periodic sparse microstrip array based on mutual coupling. *IEEE Trans Antenn Propag*, 61(4):1963-1970. https://doi.org/10.1109/TAP.2012.2235397

Reid EW, Ortiz-Balbuena L, Ghadiri A, et al., 2012. A 324-element Vivaldi antenna array for radio astronomy

instrumentation. *IEEE Trans Instrum Meas*, 61(1):241-250. https://doi.org/10.1109/TIM.2011.2159414

Sui J, Wu KL, 2017. A general T-stub circuit for decoupling of two dual-band antennas. *IEEE Trans Microw Theory Tech*, 65(6):2111-2121. https://doi.org/10.1109/TMTT.2017.2647951

Wang YW, Yu ZW, 2017. A novel symmetric double-slot structure for antipodal Vivaldi antenna to lower cross-polarization level. *IEEE Trans Antenn Propag*, 65(10):5599-5604. https://doi.org/10.1109/TAP.2017.2742543

Wang ZT, Wu Q, 2023. A novel decoupling feeding network for circularly polarized patch arrays using orthogonal mode decomposition. *IEEE Trans Antenn Propag*, 71(2):1448-1457. https://doi.org/10.1109/TAP.2022.3228693

Wheeler H, 1965. Simple relations derived from a phased-array antenna made of an infinite current sheet. *IEEE Trans Antenn Propag*, 13(4):506-514. https://doi.org/10.1109/TAP.1965.1138456

Wu KL, Wei CN, Mei XD, et al., 2017. Array-antenna decoupling surface. *IEEE Trans Antenn Propag*, 65(12):6728-6738. https://doi.org/10.1109/TAP.2017.2712818

Xia RL, Qu SW, Bai X, et al., 2014. Experimental investigation of wide-angle impedance matching of phased array using overlapped feeding network. *IEEE Antenn Wirel Propag Lett*, 13:1284-1287. https://doi.org/10.1109/LAWP.2014.2334712

Zhai GH, Chen ZN, Qing XM, 2016. Mutual coupling reduction of a closely spaced four-element MIMO antenna system using discrete mushrooms. *IEEE Trans Microw Theory Tech*, 64(10):3060-3067. https://doi.org/10.1109/TMTT.2016.2604314

Zhang SH, Chen YK, Yang SW, 2023. An extremely wideband tightly coupled dipole array with shared-aperture configuration. *IEEE Antenn Wirel Propag Lett*, 22(6):1366-1370. https://doi.org/10.1109/LAWP.2023.3242271

Zhao LY, Yeung LK, Wu KL, 2014. A coupled resonator decoupling network for two-element compact antenna arrays in mobile terminals. *IEEE Trans Antenn Propag*, 62(5):2767-2776. https://doi.org/10.1109/TAP.2014.2308547

Zhu YF, Chen YK, Yang SW, 2021. Cross-band mutual coupling reduction in dual-band base-station antennas with a novel grid frequency selective surface. *IEEE Trans Antenn Propag*, 69(12):8991-8996. https://doi.org/10.1109/TAP.2021.3098514

Zou XJ, Wang GM, Wang YW, et al., 2019. An efficient decoupling network between feeding points for multielement linear arrays. *IEEE Trans Antenn Propag*, 67(5):3101-3108. https://doi.org/10.1109/TAP.2019.2899039

Zou XJ, Wang GM, Kang GQ, et al., 2023. Wideband coupling suppression with neutralization-line-incorporated decoupling network in MIMO arrays. *AEU-Int J Electron Commun*, 167:154688. https://doi.org/10.1016/J.AEUE.2023.154688

List of supplementary materials

1 PCN for the three-element linear array

2 PCN for the five-element linear array

Fig. S1 *S*-parameters, phase differences, and prototype of the original three-element H-plane antenna array

Fig. S2 The proposed PCN for the three-element H-plane antenna array

Fig. S3 *S*-parameters, phase differences, and prototype of the three-element H-plane antenna array with the PCN

Fig. S4 Simulated and measured normalized radiation patterns of the three-element H-plane antenna array without or with the PCN

Fig. S5 Simulated and measured gains and radiation efficiencies of the three-element H-plane antenna array without or with the PCN

Fig. S6 *S*-parameters, ARCs, phase differences, and prototype of the original five-element H-plane antenna array

Fig. S7 The proposed PCN for the five-element H-plane antenna array

Fig. S8 *S*-parameters, ARCs, phase differences, and prototype of the five-element H-plane antenna array with the PCN

Fig. S9 Scanning characteristics of the five-element H-plane antenna array with the PCN

Fig. S10 Normalized scanning radiation patterns of the five-element H-plane antenna array with the PCN